Streamline-Traced, External-Compression Supersonic Inlets for Mach 2

John W. Slater
John.W.Slater@nasa.gov
NASA John H. Glenn Research Center at Lewis Field
Inlets and Nozzles Branch, Propulsion Division, Research and Engineering Directorate
Cleveland, Ohio
United States of America

ABSTRACT

A computational study was performed to explore the aerodynamic design and performance of streamline-traced, external-compression (STEX) inlets for Mach 2.0. The performance metrics included inlet flow rates, total pressure recovery, and total pressure distortion. The study explored the use of round and flattop capture cross-sections, bleed slots, and porous bleed regions. The design of the inlet and generation of the inlet geometry was performed using the Supersonic Inlet Design and Analysis (SUPIN) Tool. Computational grids were generated, and methods of computational fluid dynamics (CFD) were applied to solve the steady, three-dimensional, turbulent flow through the inlets using the Wind-US CFD flow solver. It was found that at a Mach 2 freestream, the use of a bleed slot with about 5% bleed resulted in an inlet total pressure recovery of 95% with acceptable radial and circumferential total pressure distortion. Similar performance was achieved with the use of porous bleed. It was also found that there was only a slight decrease in performance between a round and flattop capture cross-section. This suggests that the use of streamline tracing offers flexibility in shaping the inlet capture cross-section for a more favorable integration with an aircraft wing or fuselage. This flexibility and the good performance of the inlet provides a novel inlet design for future commercial supersonic aircraft.

Keywords: Supersonic Inlet; Computational Fluid Dynamics; Internal Aerodynamics

NOMENCLATURE

BC	Boundary Condition
DPC/P	SAE ARP 1420 circumferential distortion index
DPR/P	SAE ARP 1420 radial distortion index

Symbols

a_{ST}	Length of semi-major axis of tracing curves
A_1, A_{SD}, A_2	Cross-sectional area at the inlet stations
A_{cap}	Reference capture area
b_{STtop}, b_{STbot}	Length of semi-minor axis of tracing curves
D_2	Diameter of the engine face
h_0	Altitude
L_{inlet}	Length of the inlet
M_0	Freestream Mach number
M_2	Engine-face Mach number
M_{stex}	Mach number at Busemann outflow conical shock
p_{STtop}, p_{STbot}	Super-ellipse parameter
p_{t0}	Freestream total pressure
p_{t2}	Average engine-face total pressure
R_{STtop}, R_{STbot}	Aspect ratio of super-ellipse, $R = b / a$
T_0	Freestream static temperature
W_2	Engine-face flow rate
W_{bleed}	Flow rate through the bleed slot or region
W_{cap}	Reference capture flow rate
W_{C2}	Engine-face corrected flow rate
W_{C2*}	Engine-face corrected flow rate for the inlet design condition
$W_{spillage}$	Flow rate of spillage past the cowl lip
x, y, z	Cartesian coordinates
β_{stex}	Angle of Busemann outflow conical shock
θ_{stle}	Slope of leading edge of inlet

1.0 INTRODUCTION

Streamline-traced, external-compression (STEX) inlets are being studied for use in the propulsion system for future commercial supersonic aircraft for flight speeds of Mach 2. STEX inlets have an external supersonic diffuser that is shaped from the tracing of streamlines through a compressive, supersonic parent flowfield [1,2]. The inward-turning nature of the supersonic compression results in near-zero external cowl angles, which can significantly reduce the cowl wave drag compared to the wave drag of traditional two-dimensional or axisymmetric-spike inlets [1,3]. The leading edge of the inlet is swept rearward (i.e., scarfed). The terminal shock is located near the end of the external supersonic diffuser such that the subsonic spillage past the cowl lip is localized to a small segment of the circumference of the cowl lip. This can allow the inlet to be integrated with the aircraft in such a manner as to control the interaction of the spillage with the aircraft surfaces. The low external cowl angles and localized subsonic spillage also reduce and localize external pressure disturbances that can contribute to sonic boom, which would be beneficial to future commercial supersonic aircraft that will be designed for supersonic flight over populated regions [1,4].

In earlier work, a computational study was performed in which a STEX inlet was integrated with a low-boom supersonic concept aircraft [4]. It was found that the STEX inlet produced a slight reduction in aircraft drag compared to a traditional axisymmetric-spike inlet when integrated with the aircraft. The resulting sonic boom disturbances showed very little difference between the two inlets. One conclusion was that the inlet performance and sonic boom was highly dependent on the integration of the inlet within the entire supersonic aircraft flowfield [4]. One concern with the STEX inlets was that the total pressure recoveries were lower and total pressure distortions were higher in comparison with an axisymmetric-spike inlets designed for the same conditions [1,3]. This was mainly due to a more adverse terminal shock / boundary layer interaction within the STEX inlet. The interaction was followed by a localized outward-turning of the flow into the subsonic diffuser, which created a low-momentum region within the upper surfaces of the subsonic diffuser [1,3,4].

One approach studied for improving the internal flowfield was to introduce porous bleed within the throat section downstream of the terminal shock / boundary layer interaction [3]. Another approach studied was to introduce vortex generators to redistribute the low-momentum flow and reduce total pressure distortion at the engine face [5,6]. Both approaches yielded slightly improved performance for the STEX inlets.

This paper discusses the aerodynamic design of STEX inlets for Mach 2, which was the speed of the Concorde and may be the speed of interest for future commercial supersonic aircraft. The use of a bleed slot within the inlet of the Concorde was considered essential to the high performance of that inlet [7]. An objective of current work was to understand the potential performance of STEX inlets at Mach 2 with the use of a bleed slot. Further, the study compared round and flattop capture cross-sections. The flattop capture cross-section was of interest because it was expected to provide better integration of the inlet with a wing or fuselage.

Section 2.0 discusses the approach and methods used for the design of the STEX inlets. Two capture cross-section shapes were explored, one round and one flattop. Section 3.0 discusses the computational methods used to solve for the flowfield through the inlet to quantify inlet performance as measured by the inlet flow rates, total pressure recovery, and total pressure distortion. Section 4.0 discusses the results of the simulations to understand the performance of the STEX inlet at the Mach 2 design condition for variations in the capture cross-section shape and the use of a bleed slot.

2.0 STEX INLET DESIGN

This section discusses the approach and methods used to design the STEX inlets.

2.1 Freestream Conditions

The STEX inlets were considered as isolated from an aircraft such that the flow approaching the inlet was a uniform freestream with properties defined using the Standard Day Atmosphere model. The freestream state was designated with a subscript of 0 and the freestream Mach number was specified to be $M_0 = 2.0$. The altitude was specified to be $h_0 = 60000$ ft, which from the model resulted in the thermodynamic properties of p_0 = 149.78 lbf/ft^2 and T_0 = 389.97 ºR. The freestream conditions represented the upstream boundary conditions for the inlet design.

2.2 Engine-Face Geometry and Flow Rates

The downstream end of the STEX inlet is its interface with the engine, which is referred to as the engine face. An inlet design requires specification of the geometry and flow rate at the engine face. Such information forms the downstream boundary condition for the inlet design. The inlet station for the engine-face was designated with a subscript of 2. This study assumed a low-bypass turbofan engine based on the NASA Supersonic Technology Concept Aeroplanes (STCA) [8]. The STCA engine-face diameter of D_2 = 3.625 ft was considered a reasonable choice of an engine for the M_0 = 2 conditions. The engine face was assumed to have an elliptical spinner with a hub-to-tip ratio of 0.3 and aspect ratio of 2.0. The resulting engine-face annular flow area was $A_2 = 9.3918$ ft^2.

The engine-face flow rate was established by specifying the engine-face corrected flow rate, W_{C2}, which for a specified engine-face area, is equivalent to specifying the average engine-face Mach number, M_2. The choice of $M_2 = 0.50$ provided a reasonable estimate for modern low-bypass turbofan engines. For the specified A_2 and M_2, the engine-face corrected flow rate at the inlet design conditions was $W_{C2*} = 346.368$ lbm/s.

2.3 SUPIN Tool

The design of the STEX inlets and the generation of the inlet geometry were performed using the Supersonic Inlet Design and Analysis (SUPIN) Tool [9]. SUPIN used the freestream and engine-face conditions along with a set of design factors to size the inlet, estimate the inlet performance, and create the inlet geometry. SUPIN used compressible flow relations, empirical models, and computational solutions to estimate the quasi-one-dimensional flow properties through the inlet flowpath. The inlet performance was characterized within SUPIN by the inlet flow rates, total pressure recovery at the engine face, and the cowl wave drag.

2.4 STEX Inlet Design Methods

A STEX inlet was designed using streamline-tracing through a parent flowfield to construct the surface for the external supersonic diffuser. The external supersonic diffuser was then mated to a throat section and subsonic diffuser to match the specified geometry and flow rate at the engine face. The axisymmetric parent flowfield for the STEX inlet was established using the Otto-ICFA-Busemann method [2]. Figure 1 shows the features of the parent flowfield with lines representing the shock and Mach waves of the parent flowfield. The parent flowfield started with a weak oblique shock formed from a deflection caused by an internal leading-edge angle of θ_{stle} = -5.0 degrees. The internal conical flowfield A (ICFA) method was used to blend the leading-edge shock with the start of the axisymmetric Busemann flowfield. The Busemann flowfield performed an isentropic compression using Mach waves with an origin located on the flowfield axis-of-symmetry and at x = 0. The isentropic compression was terminated with a strong oblique shock with a shock angle of β_{stex}. Across the shock, the flow was decelerated to M_{stex} = 0.9 and turned into the x-direction.

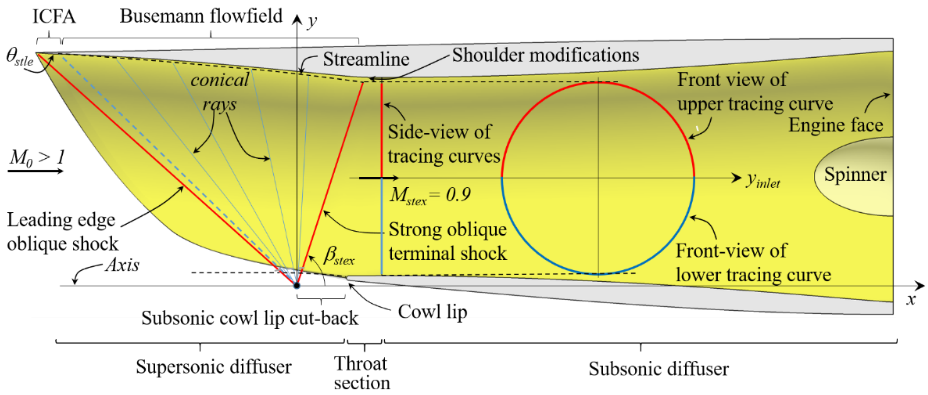

Figure 1. The features of the axisymmetric, Otto-ICFA-Busemann parent flowfield for a STEX inlet.

The surface of the external supersonic diffuser was created by tracing streamlines in the upstream direction through the parent flowfield starting from tracing curves located at the outflow of the parent flowfield. The tracing curves are shown in Fig. 1 in the side-view and front view. The center of the tracing curves was offset from the axis-of-symmetry of the parent flowfield, which resulted in a scarfed leading edge for the external supersonic diffuser. The tracing curves consisted of a top and bottom curve with shapes defined using super-ellipses. Figure 2 shows further features of the super-elliptic curves. The tracing curves have a common semi-major axis length of a_{ST}. The left image of Fig. 2 shows circular curves defined with an aspect ratio for the top and bottom curves of $R_{STtop} = R_{STbot}$ = 1.0, which indicates that the semi-minor lengths were equal to the semi-major lengths, $b_{STtop} = b_{STbot} = a_{ST}$. The circular tracing curves used values of the super-ellipse parameter $p_{STtop} = p_{STbot}$ = 2.0, which also applies for elliptical curves. The right image of Fig. 2 shows a top tracing curve with a flattop shape defined with the aspect ratio of the top curve as R_{STtop} = 0.5. The super-ellipse parameter of p_{STtop} = 3.5 also contributes to the flatness of the curve. As the super-ellipse parameter increases, the super-ellipse curve approaches a more rectangular shape.

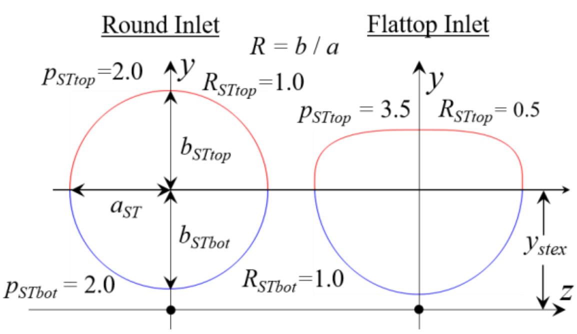

Figure 2. Factors and values used for the top and bottom tracing curves for the round and flattop STEX inlets.

The effect of the shape of the tracing curves can be seen in the images of the inlets of Figs. 3 and 4. Figure 3 is a STEX inlet with circular tracing curves. The external supersonic diffuser and throat section have circular cross-sections. Figure 4 is a STEX inlet with a flattop tracing curve. The external supersonic diffuser retains a flat shape at the leading edge. The nature of the streamline tracing resulted in a scalloped leading edge. The shape of the inlet of Fig. 4 with its flattop may provide a more favourably integrated with a wing or fuselage by allowing more of the inlet to be closer to the aircraft. The inlets created with the circular and flattop tracing curves are referred to in this study as the "round" and "flattop" inlets, respectively.

Station 1 was designated on a plane roughly normal to the flow that passes through the cowl lip, which is the portion of the leading edge of the inlet that is farthest downstream. Station 1 is represented by the dashed line in lower-left image of Fig. 3. The shoulder of the inlet is the upper segment of the internal surface of the inlet at station 1. The shoulder point occurs when the slope of the inlet surface is zero. For a STEX inlet, the terminal shock is the downstream conical shock of the parent flowfield and would be positioned about the station 1 plane. The terminal shock wraps about the cowl lip and provides a mechanism for subsonic flow within the inlet to be spilled past the cowl lip and into the external flow.

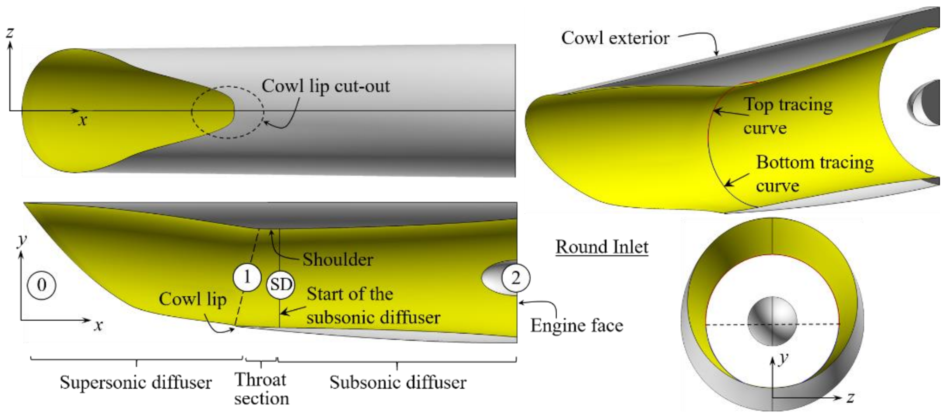

Figure 3. Views and features of the baseline round STEX inlet.

The throat section extends from station 1 to the start of the subsonic diffuser, which is designated as station SD. The throat section is a fully internal duct that has the task of taking in the flow downstream of the terminal shock and turning the flow toward the subsonic diffuser.

The shape of the throat section was initially formed as part of the streamline tracing. However, some modifications to the throat section were made to improve the flow and formating to a subsonic diffuser. The shoulder is denoted in Fig. 3 and some rounding of the shoulder was applied to smoothen the surface to avoid discrete changes in slope. Smooth surfaces are also fitted downstream of the cowl lip to further create a smooth surface for the flow into the inlet. The lines in Figs. 1, 3, and 4 that show the tracing curves are coincident with station SD, the start of the subsonic diffuser.

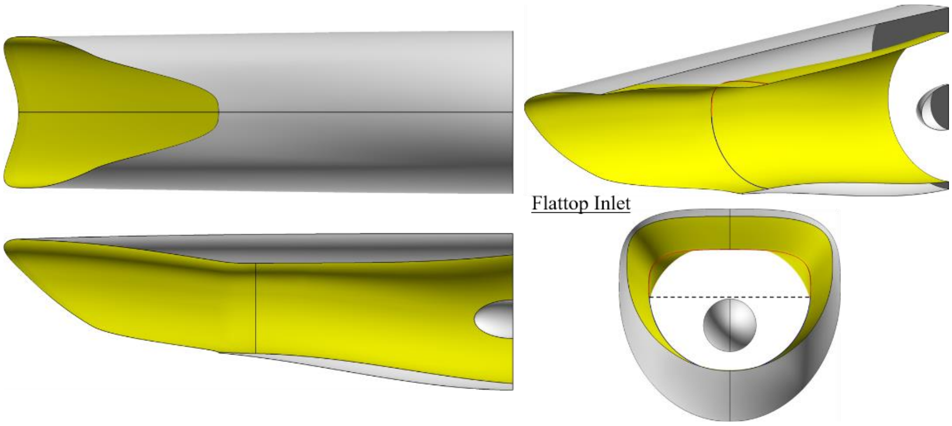

Figure 4. Views of the baseline flattop STEX inlet.

The cross-sectional area at station SD, A_{SD}, was defined through a specified area ratio A_{SD}/A_1, where A_1 is the area at the cowl entry plane. The area ratio allows the specification of some diffusion in the throat section. The axial and vertical position of the center point of station SD are specified as part of the inlet design.

A radial deformation of the shoulder was specified to increase the cross-sectional area at the shoulder plane to correct for the displacement of the boundary layer from the external supersonic diffuser. The effect of this modification is illustrated in Fig. 1 by the profile of the inlet being above the dashed curve of the streamline generated by the tracing curve.

The throat section also featured a "cut-out" at the bottom of the leading edge of the inlet. This cut-out allowed for subsonic spillage downstream of the terminal shock, which allowed for the positioning of the terminal shock with change in inlet flow rate [3]. The cut-out focuses the subsonic spillage to one region of the leading edge of the STEX inlet. This can be an advantage for the integration of the inlet with an airframe by tailoring the direction of the spillage, for example, directing the spillage away from interaction with the aircraft and directing any shocks upward to minimize their propagation towards the ground. The size of the cut-out was specified as part of the inlet design. The profile of the cowl lip was defined as an ellipse.

The subsonic diffuser extended from station SD to the engine face at station 2. The cross-sectional shapes and areas of stations SD and 2 are set by the design of the throat section and the specification of the engine face, respectively. Thus, the design factors for the subsonic diffuser mainly involve the length and area distribution of the subsonic diffuser. The length was specified as 2.5 times the engine-face diameter. The surface of the subsonic diffuser was formed as a network of NURBS curves running from station SD to the engine face about the circumference of the subsonic diffuser. The curves were specified to provide a low rate of area diffusion at the start of the subsonic diffuser, where the subsonic Mach numbers were higher than toward the engine face. The rate of area diffusion was increased in the streamwise direction toward the engine face. Examples of the surfaces of the subsonic diffusers can be seen in Figs. 3 and 4. Table 1 summarizes some of the properties of the STEX inlets.

Bleed slots were created for the inlets by specifying the streamwise and circumferential extents of the slot, which were selected to be comparable to the extent of the bleed slot of the Concorde [7]. The forward and aft lips of the slot opening were created using elliptical profiles with a specified lip thickness. A bleed plenum was constructed with a specified axial length and fitted to be packaged within the volume of the cowl exterior. The bleed slots and plenums for the round and flattop inlets are shown in Fig. 5.

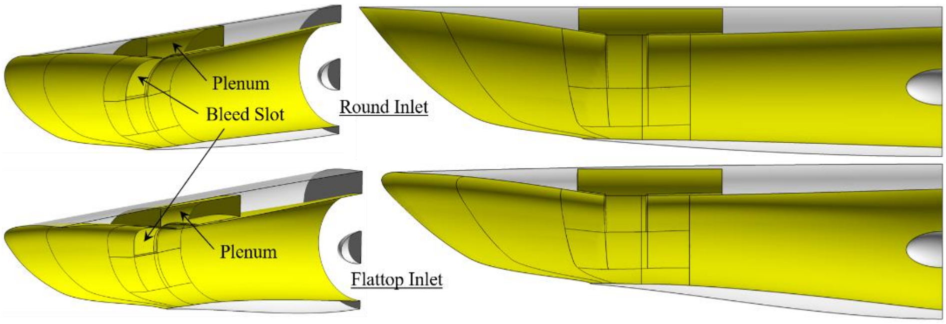

Figure 5. Views and features of the round and flattop STEX inlets with bleed slots and plenums.

Table 1. Properties of the inlets from SUPIN.

Inlet	A_{cap}/A_2	W_{bleed}/W_{cap}	p_{t2}/p_{t0}	L_{inlet}/D_2
Round: Baseline Inlet	1.151	-	0.9137	4.620
Flattop: Baseline Inlet	1.162	-	0.9229	4.315
Round: Bleed Slot	1.310	0.04	0.9099	4.858
Flattop: Bleed Slot	1.310	0.04	0.9134	4.538
Round: Bleed Region	1.310	0.04	0.9099	4.858

3.0 COMPUTATIONAL METHODS

While SUPIN was used to design the STEX inlets and provide initial estimates of the inlet performance, methods of computational fluid dynamics (CFD) were used to perform higher-fidelity analyses of the aerodynamics of the flow through the STEX inlets. The CFD solutions allowed visualization of the flowfield to better understand the shock structures, boundary layers, and other flow features within and about the inlet. From the flowfield, the inlet performance metrics were obtained.

3.1 Wind-US Flow Solver

The Wind-US CFD code [10] was used to solve the steady-state, Reynolds-averaged Navier-Stokes (RANS) equations for the flow properties at the grid points of a multi-block, structured grid for a flow domain about the STEX inlet. Wind-US used a cell-vertex, finite-volume representation for which the flow solution was located at the grid points and a finite-volume cell was formulated about the grid point. In Wind-US, the RANS equations were solved for the steady-state flow solution using an implicit time-marching algorithm with a first-order, implicit Euler method using local time-stepping. The solution process started from freestream conditions specified at all solution points. All the simulations were performed assuming calorically perfect air. The inviscid fluxes of the RANS equations were modelled using a second-order, upwind Roe flux-difference splitting method. The flow simulation can assume laminar or turbulent flow. For turbulent flow, the turbulent eddy viscosity was calculated using the two-equation Menter Shear-Stress Transport (SST) turbulence model [11]. The modelling of porous bleed regions used the Slater bleed model [12] which required specification of the boundary grid points within the bleed region and the porosity of the bleed region. The porosity is the ratio of the sum of the areas of the opening of the bleed holes over the region divided by the overall area of the bleed region on the surface. The bleed boundary condition also required specification of the static pressure of the virtual bleed plenum for the bleed region or the desired bleed rate for the bleed region.

3.2 Computational Flow Domain and Boundary Conditions

The flow domain and boundary conditions used for the CFD simulations are illustrated in Fig. 6. The flow domain shown only included half of the inlet due to geometric and flowfield symmetry about a vertical plane through the inlet at $z = 0$. The internal and external surfaces of the inlet formed a portion of the boundary of the flow domain where no-slip, adiabatic viscous wall boundary conditions were imposed. The inflow and farfield boundaries of the flow domain had freestream boundary conditions imposed in which the Mach number, pressure, temperature, angle-of-attack, and angle-of-sideslip were specified. For supersonic freestream conditions, the inflow and farfield boundaries were positioned just upstream of the leading-edge oblique shock. At the end of the cowl exterior, the domain had an external outflow boundary where an extrapolation boundary condition was applied for supersonic outflow and freestream conditions applied for subsonic outflow.

Downstream of the engine face, an outflow nozzle section was used to set the flow rate within the inlet. The use of the nozzle section moved the internal outflow boundary condition downstream of the engine face by two engine-face diameters to reduce interference of the flow at the engine face due to the application of the internal outflow boundary condition. The internal outflow boundary condition was set using a converging-diverging nozzle with a choked throat, as shown in Fig. 6. This created a non-reflective, supersonic condition at the internal outflow boundary for which an extrapolation boundary condition was applied. The inlet flow rate was set by the cross-sectional area of the nozzle throat.

For the inlets with a bleed slot and plenum, no-slip adiabatic, viscous wall boundary conditions were imposed for the surfaces of the slot and plenum. A portion of the rearward surfaces of the plenum was specified with a subsonic outflow boundary condition with the static pressure specified at those boundaries. The specified static pressure was assumed to be the bleed plenum pressure which worked to extract bleed flow through the slot and into the plenum. The bleed flow then exited the plenum through the subsonic outflow boundary. For inlets with a porous bleed region, the grid points within the bleed region were imposed as a bleed boundary condition.

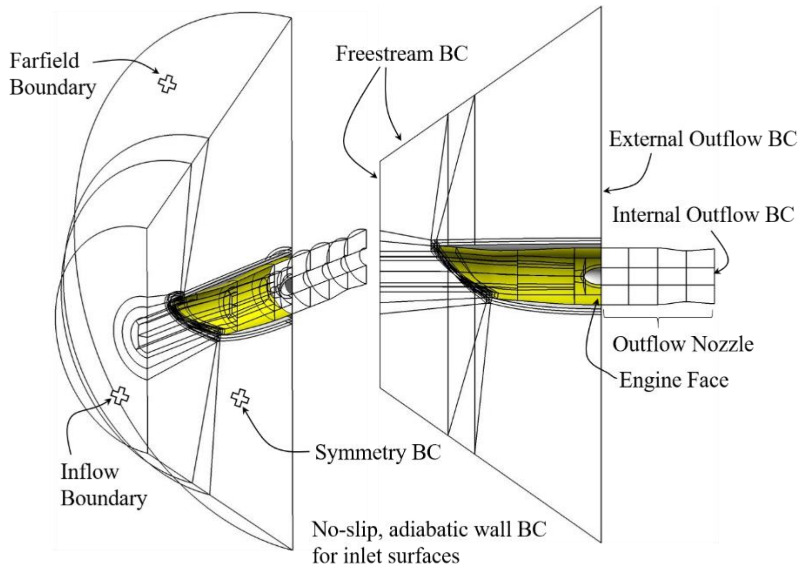

Figure 6. The flow domain and boundary conditions for the CFD simulations of the STEX inlets.

3.3 Computational Grid

Multi-block, structured grids were generated using SUPIN for the flow domain with the specification of the grid spacing inputs. The number of grid points along the edges and surfaces of the inlet were established withing SUPIN and the volume grids formed from the surfaces. SUPIN also created the boundary condition file for Wind-US. The spacing of the first point off the wall was 0.00002 ft, which resolved viscous boundary layers to $y^+ < 1$. A grid stretching ratio of 1.15 was used to distribute grid points through the boundary layer. The maximum streamwise and cross-stream grid spacings of 0.09 ft was specified within the throat section. That grid spacing was established from a grid convergence study. The specified grid spacing inputs created grids with a minimum of 210 grid points in the streamwise direction in the interior duct from the cowl lip to the engine face, 230 grid points from the bottom of the throat section to the top at the symmetry plane, and 103 grid points about the circumference of the throat section. The resulting volume grid within the internal duct of the inlet included about 5 million grid points. The number of grid points were much greater when the bleed slot was included because of smaller grid spacings within the plenum.

3.4 Inlet Performance Metrics

The first metric of inlet performance was the engine-face flow ratio, which was defined as the rate of mass flow passing through the engine face divided by the reference capture flow rate (W_2/W_{cap}). The engine-face flow rate (W_2) was computed from the simulation as the mass-average of the flow through each of the axial grid surfaces through the outflow nozzle section.

The second metric of inlet performance was the inlet total pressure recovery, which was calculated as the mass-averaged total pressure at the engine face divided by the freestream total pressure (p_{t2}/p_{t0}).

The third and fourth metrics of inlet performance were descriptors of the radial and circumferential total pressure distortion at the engine face as represented by the indices DPR/P and DPC/P, respectively. The indices were computed using the methods of the Society of Automotive Engineers (SAE) Aerospace Recommended Practices (ARP) 1420 document [13]. The indices were computed from total pressures interpolated from the CFD simulation onto the probe locations of a virtual 40-probe rake as defined according to the SAE ARP 1420. The rake consisted of eight arms with five probes per rake. The probes were positioned along each arm such that their radial position was at the centroid of equal areas of the annular disk at the engine face.

3.5 Iterative Convergence

Iterative convergence of each flow simulation was evaluated through monitoring convergence of the inlet flow rate, total pressure recovery and distortion. The steady-state solution was considered converged when these values varied less than 0.01% of their values over hundreds of iterations. The solution residuals were also monitored to check that they reduced and approached steady-state values.

4.0 RESULTS

The flow simulations focused on comparing the performance of the round and flattop inlets and evaluating the effectiveness of the bleed slot.

4.1 Baseline Inlets at the Critical Flow Conditions

An understanding of the fundamental behavior of the STEX inlet flow can be obtained from CFD simulations of the baseline round and flattop inlets with the inlet operating at the critical flow condition. The critical flow condition occurs when the corrected flow rate at the engine face (W_{C2}) matches the design corrected flow rate (W_{C2*}). The operating condition of the inlet can be expressed by the engine-face corrected flow ratio (W_{C2}/W_{C2*}). The critical flow condition is $W_{C2}/W_{C2*} = 1.0$. Subcritical conditions correspond to $W_{C2}/W_{C2*} < 1$ and supercritical conditions correspond to $W_{C2}/W_{C2*} > 1$.

Figure 7 shows Mach number contours of the resulting flowfields for the baseline round and flattop inlets operating at the critical flow condition. Shown are the Mach number contours at the inlet symmetry plane and at several axial planes through the inlet. Both flowfields show the terminal shock positions about the station 1 plane. The terminal shock is inclined toward the downstream direction about the cowl lip such that it interacts with the shoulder, which is the desired position. A small supersonic region forms just downstream of the point of interaction of the terminal shock with the shoulder. Downstream of the shoulder interaction, the boundary layer thickens to form a region of low-momentum flow. For the round inlet, the low-momentum flow gathers mostly about the top of the subsonic diffuser. For the flattop inlet, the low-momentum flow gathers toward the curved “corner” of the cross-section of the forward part of the subsonic diffuser. The low-momentum flow does not include any separation but does continues toward the engine face and introduces total pressure losses.

The inlet performance metrics for the simulations of the baseline round and flattop inlets at the critical flow conditions are listed in Table 2. The inlet total pressure recoveries of $p_{t2}/p_{t0} = 0.8774$ and 0.8732 for the round and flattop inlets, respectively, are well below the MIL-E-5007 [14] expected recovery of $p_{t2}/p_{t0} = 0.92$. The radial and circumferential distortion indices of DPR/P ≈ 0.1 and DPC/P ≈ 0.1, which are about the acceptable upper limit for the distortion indices and much greater than desired. The similar performance between the round and flattop inlets provides some confidence that an inlet designer has flexibility in selecting a desirable capture cross-section shape to improve integration of the inlet with the aircraft.

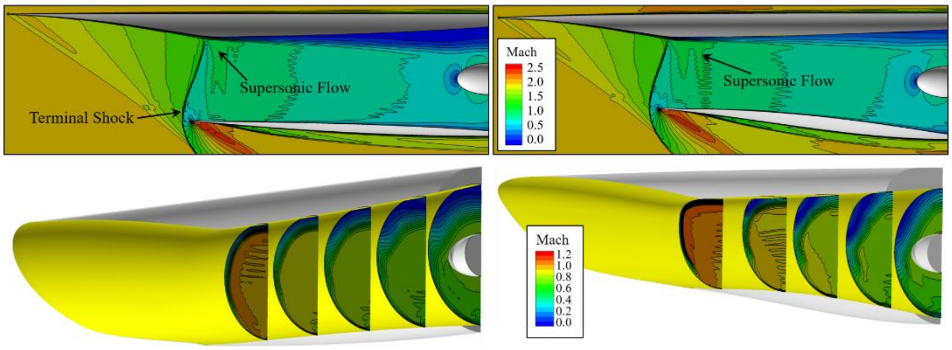

Figure 7. Mach number contours on the symmetry plane (top) and at axial stations (bottom) for the baseline round (left) and flattop (right) STEX inlets with the inlet flow at the critical operating condition.

Table 2. Performance of the STEX inlets at the critical operation condition.

Inlet	$W_{spillage}/W_{cap}$	W_{bleed}/W_{cap}	W_2/W_{cap}	p_{t2}/p_{t0}	DPR/P	DPC/P
Round: Baseline Inlet	0.0425	-	0.9575	0.8774	0.0900	0.1030
Flattop: Baseline Inlet	0.0526	-	0.9474	0.8732	0.1145	0.0939
Round: Bleed Slot	0.0376	0.0504	0.9120	0.9490	0.0493	0.0328
Flattop: Bleed Slot	0.0390	0.0518	0.9092	0.9456	0.0567	0.0285
Round: Bleed Region	0.0346	0.0517	0.9137	0.9527	0.0478	0.0323

4.2 Inlets with Bleed Slots at the Critical Flow Condition

CFD simulations were performed of the round and flattop inlets with the bleed slots and with the inlet flow rate at the critical flow condition. A slot bleed rate of W_{bleed}/W_{cap} = 0.0517 was specified for both inlet simulations. Figure 8 shows Mach number contours at the inlet symmetry plane and at several axial planes through the inlet of the resulting flowfields for the round and flattop inlets with the bleed slots. The flowfield images show the terminal shock was pulled into the inlet and toward the downstream direction by the action of the bleed slot. A sizable supersonic region formed below the bleed slot and downstream where the terminal shock interacts with the bleed slot. The supersonic region ends with a normal shock that sits at the end of the bleed slot; however, the normal shock does not span the entire height of the inlet. Most of the bleed flow was extracted from the core inlet flow by a jet of airflow positioned at the end of the bleed slot that was directed into the bleed plenum. This scenario of the terminal shock, internal supersonic region, and jet of bleed airflow is similar to that of the inlet for the Concorde aircraft [7]. Downstream of the bleed slot, the flow is subsonic as it continues to diffuse toward the engine face. The bleed slot removed much of the low-momentum flow observed for the baseline inlets; however, the round inlet with the bleed slot does seem to retain some low-momentum flow at the top of the subsonic diffuser. Some low-momentum flow and a vortex does seem to form where the bleed slot ends in the circumferential direction (i.e., side of the inlet). This low-momentum vortex flow seems to be larger for the flattop inlet, and for both inlets, the vortex propagates down the subsonic diffuser all the way to the engine face. Even with the vortex, the flow seems rather uniform at the engine face.

The inlet performance metrics for the simulations of the round and flattop inlets with the bleed slot at the critical flow conditions are listed in Table 2. The inlet total pressure recoveries of p_{t2}/p_{t0} = 0.9490 and 0.9456 for the round and flattop inlets, respectively, and well above the MIL-E-5007 expected recovery of $p_{t2}/p_{t0} = 0.92$. The radial and circumferential distortion indices of DPR/P ≈ 0.05 and DPC/P ≈ 0.03, which are very acceptable levels of distortion. These performance metrics show a dramatic improvement over the values for the baseline inlets.

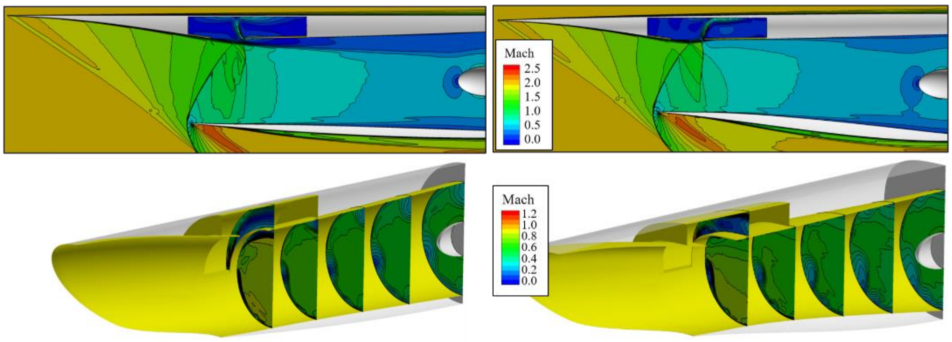

Figure 8. Mach number contours on the symmetry plane (top) and at axial stations (bottom) for the round (left) and flattop (right) inlets with bleed slots with inlet flow at the critical operating condition.

4.3 Round Inlet with a Porous Bleed Region

Simulations were performed with the round inlet with a porous bleed region rather than a bleed slot. The inlet geometry was the same as the round inlet with the bleed slot of the previous subsection and shown in Fig. 5, but the slot was not included. The porous bleed region was specified to extend over the same region as the opening of the bleed slot. The porous bleed region was specified to have normal bleed holes and a porosity of 40%. The bleed rate for the bleed region was specified to be the same as the simulations of the previous subsection with $W_{bleed}/W_{cap} = 0.0517$.

Figure 9 shows Mach number contours of the resulting flowfield. Shown are the Mach number contours at the inlet symmetry plane and at several axial planes through the inlet. The flowfield images show similarities in the structure of the terminal shock and internal supersonic region to the images for the round inlet with a bleed slot shown in Fig. 8. The lower resolution of the shocks in Fig. 9 are due to less grid resolution than the image of Fig. 8, which used a grid with finer resolution of the region about the bleed slot. The Mach number contours on the axial planes of Fig. 9 show a similar structure of the low-momentum vortex flow at the spanwise end of the bleed region as shown in Fig. 8 for the round inlet with a bleed slot.

The inlet performance metrics for the simulation are listed in Table 2. The values of $p_{t2}/p_{t0} = 0.9527$, DPR/P = 0.0478, and DPC/P = 0.0323 are similar to those of the round inlet with the bleed slot. These results suggest that the use of a porous bleed region rather than a bleed slot may be an acceptable option.

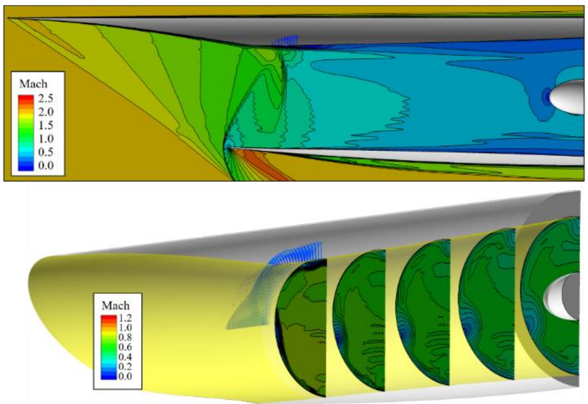

Figure 9. Mach number contours on the symmetry plane (top) and at axial stations (bottom) for the round inlet with a porous bleed region with inlet flow at the critical operating condition.

4.4 Inlet Characteristic Curves

CFD simulations were performed for each of the inlets to obtain the characteristic curves relating the variation of the inlet total pressure, distortion, spillage, and bleed properties over a range of engine-face flow ratios. The engine-face flow ratios were varied through the change of the cross-sectional area of the throat of the outflow nozzle, as described in subsection 3.2. The simulations started with the supercritical condition and continued in sequence to the subcritical condition.

The characteristic curves of the inlet total pressure recovery with respect to the engine-face flow ratio are shown in the plots on the left side of Fig. 10. The dashed line represents the MIL-E-5007 [14] goal of recovery for an inlet at Mach 2. The characteristic curve consists of a supercritical leg and a subcritical leg that connect at the critical point. The supercritical leg is mostly vertical, which indicates nearly constant engine-face flow ratio. The subcritical leg is mostly horizontal, which indicates nearly constant inlet total pressure recovery. This shape of the characteristic curve results in it also being referred to as a “cane” curve. The critical point exhibits almost maximum engine-face flow ratio and maximum total pressure recovery. The critical point is referred to as the “knee” of the characteristic curve. With the correct sizing of the inlet, the engine-face corrected flow rate at the critical point would match the design engine-face corrected flow rate.

The characteristic curves for the baseline round and flattop inlets show the expected “cane” shape of the characteristic curves and the recoveries are well below the MIL-E-5007 recovery. The characteristic curves for the inlets with the bleed slot and bleed region show a less defined knee of the curve due to the gradual change in the bleed rate as the engine-face flow ratio is varied. The recoveries for these inlets exceed the MIL-E-5007 recovery by almost 4%. The curves are of similar form for the round and flattop inlets.

The plots to the right in Fig. 10 show the variation of the ratio of the spillage flow past the cowl lip. For the baseline inlets, the inlet spillage varies linearly with engine flow with greater spillage as the engine flow is reduced. The greater amount of spillage is accompanied by a forward motion of the terminal shock to allow the increased amount of subsonic spillage past the cowl lip. This movement of the terminal shock is illustrated below in the discussion of Fig. 13. For the inlets with a bleed slot or bleed region, the plots on the right of Fig. 10 show that the spillage remains essentially fixed over the range of engine flow ratios, which is a desirable characteristic.

The curves of Fig. 11 show the SAE 1420 radial and circumferential distortion indices for the inlets over the simulated range of engine flow ratios. The dashed lines indicate the upper limit of acceptable distortions. The distortion indices for the baseline inlets straddled the limit line and likely would not provide a margin against unacceptable distortion for a turbofan engine. The distortion indices for the inlets with a bleed slot or porous bleed region showed a range of radial distortion indices of mostly $0.04 \leq DPR/P \leq 0.06$ and circumferential distortion indices of mostly $0.02 \leq DPC/P \leq 0.04$, which would likely be acceptable with margin for a turbofan engine.

The curves of Fig. 12 show the bleed ratios and plenum pressure ratios for inlets with a bleed slot or region. The curves on the left in Fig. 12 show a nearly linear variation of the bleed ratio with engine-face flow ratio. For the simulations, the bleed ratios were specified for each outflow nozzle setting to allow for direct comparison of the performance of the round and flattop inlets. The values of the bleed ratios were obtained from a set of simulations for an earlier version of the round inlet with a bleed slot. As can be seen for the plots on the left side of Fig. 12, the bleed ratios varied from just over 4% for the most-supercritical point to almost 9% for the most-subcritical point on the curve. Table 2 indicates that for the critical inlet operation, the bleed ratio was slightly over 5%. The plots on the right side of Fig. 12 indicate the plenum static pressures for the variation of engine-face flow ratios. An interesting observation is that the flattop inlet requires lower plenum pressures than those of the round inlet to extract the same amount of bleed flow. Also, the simulations of the round inlet with the porous bleed region show a nearly constant level of bleed plenum pressures.

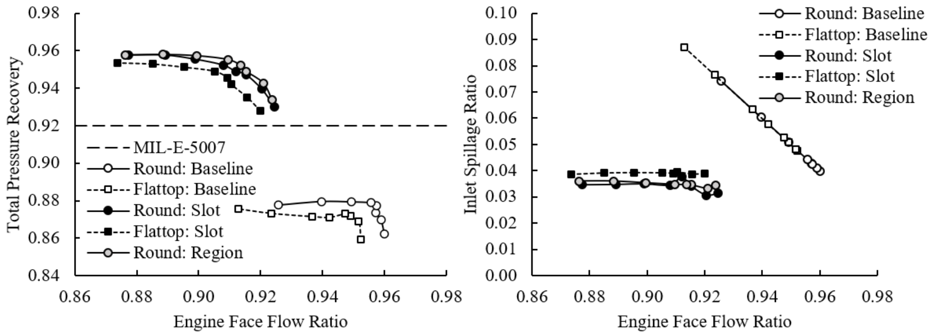

Figure 10. Characteristic curves (left) and spillage ratio curves for the inlet simulations over a range of engine-face flow ratios.

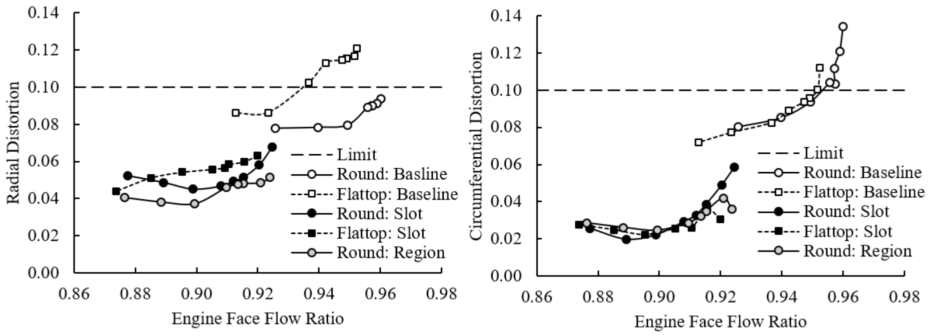

Figure 11. Curves for the SAE 1420 radial (left) and circumferential (right) distortion indices for the inlet simulations over a range of engine-face flow ratios. The dashed line suggests an upper limit on the distortion indices.

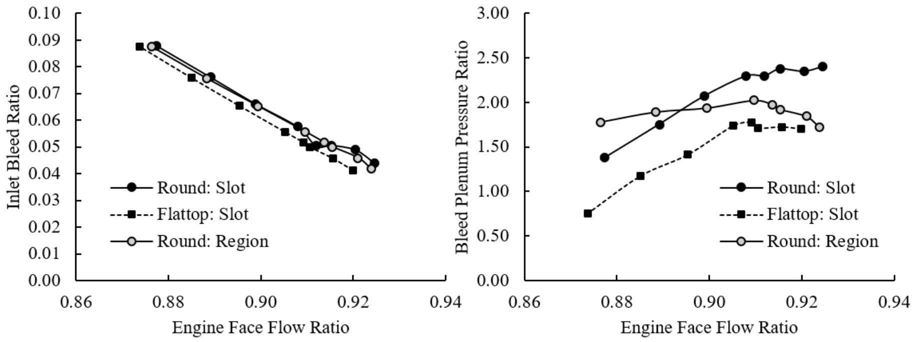

Figure 12. Curves for the variation of the inlet bleed ratio (W_{bleed}/W_2) (left) and bleed plenum pressure ratio (p_{plenum}/p_0) (right) for the inlet simulations over a range of engine-face flow ratios.

The bleed slot provides a useful control on the position of the terminal shock as the engine-face flow ratio is varied. This control is illustrated in the Mach number contours of Fig. 13 for three engine-face flow ratios for the baseline flattop inlet and the flattop inlet with a bleed slot. The values of the engine-face corrected flow ratio (W_{C2}/W_{C2*}) of Fig. 13 indicate subcritical, critical, and supercritical inlet operating conditions.

The images of the left column of Fig. 13 are from the simulations of the baseline flattop inlet without any bleed. As can be seen, as the inlet operation becomes more subcritical, the terminal shock is pushed upstream onto the external supersonic diffuser to allow the excess flow within the inlet to spill at subsonic conditions past the cowl lip. At the supercritical condition shown, the terminal shock is drawn slightly into the inlet as the amount of subsonic spillage past the cowl lip is reduced to make up for the increased engine-face flow demand.

The images on the right of Fig. 13 are for a similar range of engine-face flow ratios as the images on the left; however, the terminal shock remains essentially fixed in place.

Any change in the engine-face flow rate is matched by a corresponding change in the bleed slot flow rate. The primary difference between the images on the right of Fig. 13 can be seen downstream of the terminal shock with the change in size of the internal supersonic region and the normal shock at the end of the bleed slot. As the flow varies from subcritical to critical and then to supercritical, the size of the internal supersonic region increases and the extent of the normal shock across the height of the inlet increases. The above characteristic curves show the corresponding change in various performance metrics with the change in the engine-face flow ratio.

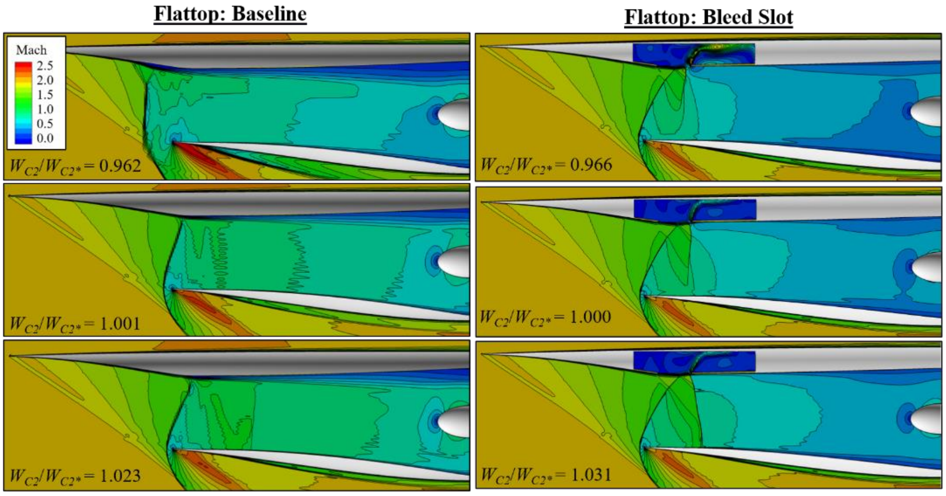

Figure 13. Mach number contours on the symmetry plane from CFD simulations for the baseline flattop inlet (left) and the flattop inlet with a bleed slot (right) over a range of engine-face corrected flow ratios flow from subcritical to supercritical inlet operation.

SUMMARY AND CONCLUSIONS

Streamline-traced, external-compression (STEX) inlets for Mach 2 have been designed using computational methods for a representative turbofan engine with an engine-face Mach number of $M_2 = 0.5$. The STEX inlet designs explored the use of round and flattop capture cross-sections. The flattop inlets feature a flattened top surface to the external supersonic diffuser, which may allow better integration with the lower or upper surface of a wing or fuselage. The results showed little difference in inlet performance with the use of a round or flattop capture cross-section. The use of a bleed slot was demonstrated to increase the total pressure recovery by almost 7% over an inlet without a bleed slot. Recoveries of about $p_{t2}/p_{t0} = 0.95$ with $W_{bleed}/W_{cap} = 0.05$ for the critical inlet operation were achieved. The use of the bleed slots reduced the formation of low-momentum flow within the subsonic diffuser, which reduced radial and circumferential distortion indices to acceptable levels. The use of the bleed slot demonstrated a stabilizing effect on the position of the terminal shock with the exchanging of bleed flow rates with engine-face flow rates. The STEX inlet with a bleed slot provides an attractive option for future commercial supersonic aircraft.

ACKNOWLEDGMENTS

The author would like to acknowledge the support of the Commercial Supersonic Technology Project of the NASA Advanced Air Vehicles Program.

REFERENCES

[1] J W SLATER, "Methodology for the Design of Streamline-Traced, External-Compression Inlets," AIAA Paper 2014-3593, July 2014.

[2] S E OTTO, C J TREFNY, and J W SLATER, "Inward-Turning Streamline-Traced Inlet Design Method Low-Boom, Low-Drag Applications," *AIAA Journal of Propulsion and Power*, Vol. 32, No. 5, pp. 1178-1189, 2016.

[3] J W SLATER, "Enhanced Performance of Streamline-Traced External-Compression Supersonic Inlets," ISABE-Paper 2015-22049, October 2015.

[4] C M HEATH, J W SLATER, S K RALLABHANDI, "Inlet Trade Study for a Low-Boom Aircraft Demonstrator," AIAA Paper 2016-4050, June 2016.

[5] E BAYDAR, F K LU, J W SLATER, and C J TREFNY, "Vortex Generators in a Streamline-Traced, External-Compression Supersonic Inlet," AIAA Paper 2017-1383, January 2017.

[6] J W SLATER, "Refinement of Vortex Generators in a Streamline-Traced, External-Compression Supersonic Inlet," AIAA Paper 2019-4423, August 2019.

[7] J W SLATER, "A Study of the Internal Aerodynamics of the Concorde Inlet," AIAA Paper 2020-3770, August 2020.

[8] J J BERTON, D L HUFF, J A SEIDEL, AND K A GEISELHART, "Supersonic Technology Concept Aeroplanes for Environmental Studies," AIAA Paper 2020-0263, January 2020.

[9] J W SLATER, "SUPIN: A Computational Tool for Supersonic Inlet Design," AIAA Paper 2016-0532, January 2016.

[10] D A YODER, "Wind-US User's Guide: Version 4.0," NASA TM 2016-219145, September 2016.

[11] F R MENTER, "Two-Equation Eddy-Viscosity Turbulence Models for Engineering Applications," *AIAA Journal*, Vol. 32, No. 8, pp. 1598-1605, 1994.

[12] J W SLATER, "Improvement in Modeling 90-degree Bleed Holes for Supersonic Inlets," *AIAA Journal of Propulsion and Power*, Vol. 28, No. 4, pp 773-781, 2012.

[13] SOCIETY OF AUTOMOTIVE ENGINEERS (SAE), "Gas Turbine Engine Inlet Flow Distortion Guidelines," SAE ARP 1420, Rev. C, April 2017.

[14] MIL-E-5007E, "Engines, Aircraft, Turbo-Jet, and Turbofan, General Specifications For," September 1983.